Science Advances
AAAS

Supplementary Materials for

Highly oxidized intraplate basalts and deep carbon storage

Xu-Han Dong *et al.*

Corresponding author: Shui-Jiong Wang, wsj@cugb.edu.cn; Wenzhong Wang, wwz@ustc.edu.cn

Sci. Adv. **10**, eadm8138 (2024)
DOI: 10.1126/sciadv.adm8138

The PDF file includes:

Other Supplementary Material for this manuscript includes the following:

Supplementary Text

Supplementary Section 1

Geological Setting and samples

Cenozoic intraplate basalts in eastern China are widely distributed along the coastal provinces and adjacent offshore shelf extending over 4000 km. Representative Cenozoic intraplate basalts from eight localities in eastern China were analyzed for $Fe^{3+}/\sum Fe$ value in this study. In a total alkali vs silica (TAS) diagram, studied samples ranges from nephelinite to basaltic andesite (Fig. S1). Their FeO_{total} range from 9.7 to 14.5 wt% (*77-82*).

Datong volcanic field (DVF) is located in the northern part of the Trans-North China Orogen. The DVF erupted at 0.74 Ma and 0.4 Ma (*83, 84*). Eighteen fresh samples analyzed herein are porphyritic olivine basalts, where phenocrysts are olivine, plagioclase and clinopyroxene, and the groundmass is composed of plagioclase, clinopyroxene and needle-shaped Fe–Ti oxide (*77*). These samples range from tholeiitic basalt, alkaline trachybasalt to basanite (*77*), with their major, trace element and Mg-Zn isotopic compositions reported in Wang and Liu (*77*).

Hannuoba basaltic plateau is located along the northern margin of the Trans-North China Belt. Hannuoba basalts have K-Ar ages of 14-22 Ma (*78*). Five samples from Hannuoba analyzed in this study are porphyritic alkaline basalts (*78*). They have rare and small fresh olivine phenocrysts with a groundmass of plagioclase, clinopyroxene, olivine, and opaque minerals (*78*). Their major and trace elements have been studied by Qian et al. (*78*), and Mg isotopic compositions were reported in Li et al. (*16*).

Shandong basaltic field is located in the North China carton. The Cenozoic alkaline magmatism in Shandong took place during two periods: 24.0-10.3 Ma and 8.7-0.3 Ma (15, *85*). The early magmatism was voluminous and characterized by large volcanoes densely distributed in a narrow area near the Tan-Lu Fault. Most samples are fresh except a few samples from Fangshan and Mashan, whose olivine phenocrysts are partially altered to iddingsite (*79*). All samples have minor olivine as phenocrysts in a groundmass of olivine, Ti-magnetite, nepheline, and glass (*79*). These samples are classified as basanite and nephelinite (*79*). Their $Fe^{3+}/\sum Fe$ have been analyzed by Sheng et al. (*86*), and our duplicated analyses of $Fe^{3+}/\sum Fe$ for a selective set of samples agree well within 3% with those reported in Sheng et al. (*86*) (Table S1). Comparison of $Fe^{3+}/\sum Fe$ values between unaltered and slightly altered samples suggests that iddingsitization does not have an impact on the bulk-rock $Fe^{3+}/\sum Fe$ (*86*). Their major and trace element compositions were reported by Zeng et al. (*15*) and Zeng et al. (*79*), and their Mg-Zn isotope were reported in Zeng et al. (*79*) and Wang et al. (*87*).

Pingmingshan – Anfengshan is located in the Sulu orogenic belt. Pingmingshan and Anfengshan basalts have K-Ar ages of 7.3-12.3 and 4.0-6.4 Ma, respectively (*85*). Five samples from Pingmingshan and three samples from Anfengshan were analyzed

in this study. Most of the studied samples are fresh, except for 13AFS9 and 13AFS10, whose olivine phenocrysts were partially altered to iddingsite. These samples are porphyritic basanite (*80*), where phenocrysts consist predominantly of olivine in the Anfengshan basalts and olivine, clinopyroxene, and plagioclase in the Pingmingshan basalts (*80*). Their groundmass mainly consists of plagioclase, olivine, augite, nepheline, magnetite and glass. Their major and trace element compositions have been studied by Huang et al. (*80*). Their Mg-Zn isotopic compositions were reported in Li et al. (*16*) and Liu et al. (*39*).

Jiaozhou is located in Jiaolai basin in the North China carton. Jiaozhou basalts have K-Ar ages of 71.9 Ma (*81*). Four samples studied in this study are porphyritic basanites (*81*), where phenocrysts consist of fresh pyroxene and olivine and groundmass mainly consists of plagioclase, olivine, pyroxene and Fe-Ti oxide (*81*). Their major, trace element and Sr-Nd isotopic compositions have been studied by Meng et al. (*81*). The Mg isotope compositions of four samples were reported in Li et al. (*16*).

Fangshan is located in the northeast of the South China Block. Fangshan basalts were dated at 2.9-3.5 Ma by K-Ar method (*80*). Five fresh samples analyzed in this study are porphyritic trachybasalt (*80*), where phenocrysts consist of olivine and clinopyroxene and the groundmass mainly consists of plagioclase, olivine, augite, nepheline, magnetite and glass. Their major, trace element and Mg-Zn isotope compositions were reported in Huang et al. (*80*) and Liu et al. (*39*).

Longyou is located in the east of the South China Block. Longyou basalts were dated at 9.4-9.0 Ma by K-Ar method (*80*). They are porphyritic basanites, and phenocrysts consist of olivine and clinopyroxene. Their groundmass mainly consists of plagioclase, olivine, augite, nepheline, magnetite and glass. Two samples from Longyou are analyzed in this study. Sample 10LYSK13 is fresh, whereas 10LYSK11 is slightly altered with olivine phenocrysts partially replaced by iddingsite. These two samples show very similar $Fe^{3+}/\sum Fe$ values of 0.33 and 0.34, respectively, supporting that iddingsitization does not change the bulk-rock $Fe^{3+}/\sum Fe$ (Table S1). Their major, trace element and Mg-Zn isotope compositions were reported in Li et al. (*16*) and Liu et al. (*39*).

Niutoushan is located in the southeast of the South China Block. Niutoushan basalts were dated at 19.2-11.7 Ma by K-Ar method (*82*). An alkaline basalt sample from Niutoushan was analyzed in this study. This sample has fresh olivine and pyroxene as phenocrysts in a groundmass of plagioclase and pyroxene (*82*). Its major and trace element compositions were reported by Yang (*82*) and Mg isotopic compositions were reported in Li et al. (*16*).

Supplementary Section 2

$Fe^{3+}/\sum Fe$ correction for crystal fractionation

Different degree of crystal fractionation prior to eruption may cause the $Fe^{3+}/\sum Fe$ variation, although this effect is thought to be minimal (*88*). Here, we corrected $Fe^{3+}/\sum Fe$ data to the primary magma composition, following the method of Sossi et al. (*89*). Since all of our studied basalts have MgO > 6 wt%, it is assumed that olivine is the only crystal phase removed from or added to the melts (*89*). Olivine in equilibrium with melt is calculated using $K_{D\,Ol-Melt}^{Fe-Mg} = 0.3$ (defined as the molar Fe^{2+}/Mg of the liquid divided by Fe/Mg of coexisting olivine (*90*)), and it is added or subtracted at a step of 1 wt% until $Mg\#_{melt} = 0.72$, equilibrium with mantle olivine at Fo_{90}. Considering that olivine in an oxidized mantle may have a lower Fo content than the normal mantle (*91*), we did another set of correction to equilibrate the melt with mantle olivine at Fo_{85}. The MgO and FeO composition of the olivine crystallizing is given by:

$$\left(\frac{Fe}{Mg}\right)_{Ol} = K_{D\,Ol-Melt}^{Fe-Mg}\left(\frac{Fe}{Mg}\right)_{Melt}$$

where Fe = FeO (wt%)/71.845 and Mg= MgO (wt%)/40.3. The composition of the olivine is iterated every 1%, and the composition of the melt + olivine mixture is given by mass balance:

$$M_{Melt}^{F_n} = \left(1 - (F_n - F_{n-1})\right)M_{Melt}^{F_{n-1}} + (F_n - F_{n-1})M_{Ol}^{F_n}$$

M refers to the concentration of an element, and F is the fraction of olivine, which ranges from $F_1, F_2 \ldots F_n$, where n is the number of iterations. The modelling results show that olivine fractional crystallization or accumulation may have shifted $Fe^{3+}/\sum Fe$ data by no more than 0.08, and the corrected $Fe^{3+}/\sum Fe$ for melts equilibrated with Fo_{90} or Fo_{85} olivines agree with each other within 24% (Fig. S7).

Supplementary Section 3

Partial melting models

A non-modal batch melting model is used to evaluate the distribution of Fe^{2+} and Fe^{3+} during partial melting. Initial modal abundances of olivine, clinopyroxene, orthopyroxene, and garnet are assumed to be 0.53, 0.27, 0.18, and 0.02, respectively (*92*). Melting reactions of partial melting of garnet peridotite were taken from Walter et al. (*92*). Garnet and clinopyroxene in peridotite were modeled to be exhausted at 10% and 23% degree of melting. Partition coefficients for Fe^{2+} ($D_{Fe^{2+}}$) and Fe^{3+} ($D_{Fe^{3+}}$) of mantle minerals are from Wang et al. (*93*). The bulk partition coefficient (P) of the melt and solid are calculated using the partition coefficients of melt and minerals (D_{l-j}) and the relative proportion of a given mineral in the melting reaction (r_j):

$$P = \sum_{j=1}^{n} [r_j * D_{l-j}]$$

The element abundance in the melt C_i^l can be calculated using the equation of

$$C_i^l = \frac{C_i^0}{D_0 + (1-P)F}$$

where F is degree of partial melting, C_i^0 is the initial element abundance, and D_0 is the melt-solid partition coefficient at the onset of melting.

We also used a fractional melting model to determine the Fe^{2+} and Fe^{3+} content in the melts for comparison:

$$C_i^l = C_i^0 \times \frac{1}{D_0}(1 - \frac{PF}{D_0})^{(\frac{1}{P}-1)}$$

Our modelling shows that the $Fe^{3+}/\sum Fe$ value of melts does not differ significantly between batch melting and fractional melting (Fig. S8). Partial melting of a peridotitic mantle source with a normal-mantle $Fe^{3+}/\sum Fe$ of 0.036 (*28*) cannot produce the high-$Fe^{3+}/\sum Fe$ value observed in EC basalts (Fig. S8). In order to produce the high $Fe^{3+}/\sum Fe$ as high as 0.6 in EC basalts, the $Fe^{3+}/\sum Fe$ of the mantle source must be elevated to, for example, ~0.30 if 3% partial melting degree is assumed (Fig. S8).

Supplementary Section 4

Mixing model calculation

We calculate the amount of subducted carbonate required to produce the observed high-$\delta^{66}Zn$ and low-$\delta^{26}Mg$ endmember for the HOME using a mixing model of subducted oceanic crust and carbonate. Experimental studies have shown that with increasing pressure during subduction, the stable carbonate mineral changes from calcite, to calcite/dolomite, and to dolomite/magnesite (e.g. *94*). Therefore, dolomite/magnesite was taken as an endmember in the mass balance calculations. The subducted oceanic crust is assumed to be a mixture of carbonate minerals and MORB. The modelling results are plotted in Fig. S10.

Our modelling suggests that involving small amounts of dolomite and magnesite in the melting reactions would lead to a significant deviation of the Mg-Zn isotopic compositions of the melt from the normal mantle range, and different carbonate species have different effects on the Mg-Zn isotopic compositions of resulting melts due to the distinct elemental contents and initial isotopic compositions of dolomite and magnesite. Overall, in order to produce the observed high-$\delta^{66}Zn$ and low-$\delta^{26}Mg$ HOME, 10-20% of carbonates are needed in the melting reaction during the partial melting of carbonated oceanic crust (Fig. S10A).

The Mg-Zn isotopic variations observed in the EC basalts can be explained by a mixture of the HOME (15% carbonate + 85% MORB) and asthenospheric peridotite (Fig. S10B). Modelling parameters are provided in Supplementary Table 7.

Supplementary Section 5

Computational details of the melt-diamond density crossover at mantle depth

We performed first-principles molecular dynamics (FPMD) simulations based on density functional theory (DFT) using the Vienna *ab initio* simulation package (VASP). The local density approximation (LDA) and projector augmented wave method were adopted for the exchange-correlation functional. The energy cutoff was 600 eV. The gamma point was used for Brillouin zone summations over the electronic states. Previous studies found that LDA works better than the generalized gradient approximation (GGA) in predicting many properties of silicates including equation of state and elasticity (*95-97*). Single-particle orbitals were populated based on the Fermi–Dirac statistics. All spin-polarized FPMD simulations were performed in the NVT (constant number of atoms N, volume V, and temperature T) thermodynamic ensemble with a fixed temperature controlled by a Nosé thermostat. The time step was set to 1 fs. We focus on three types of silicate melts with mid-ocean ridge basalt (MORB) compositions, $Mg_6Ca_6Fe_5Si_{27}Al_{10}Na_3O_{88}$ (dry MORB), $Mg_6Ca_6Fe_5Si_{27}Al_{10}Na_3H_{18}O_{97}$ (MORB with 4.9 wt.% water), and $Mg_6Ca_6Fe_5Si_{27}Al_{10}Na_3C_4O_{96}$ (MORB with 5.3 wt.% CO_2) to model the water- and carbon-bearing basaltic melts (Table S5). We did not introduce a Hubbard U correction for Fe atoms, as Caracas et al. (*98*) found that a +U correction does not significantly improve the calculated properties. The initial melt configurations at different volumes were prepared by melting the structures at 6000 K and down to 3000 K for 10 ps, and then, we ran NVT simulations at 1700 K for at least 40 ps. Pressures at different volumes were derived by averaging the pressure for each time step after the equilibration. The calculated results together with the chemical compositions were listed in Table S6.

Our calculated results show that at 1700 K, the density of dry basaltic melt increases from 3.046 g/cm^3 at 2.2 GPa to 3.461 g/cm^3 at 7.5 GPa. A linear interpolation suggests a density of ~ 3.35 g/cm^3 at 6 GPa, which is higher than the measured values (3.23 g/cm^3) at 5.9 GPa and 1673 K using the sink-float method (*99*). This is typical for the LDA, which underestimates the volumes of silicate minerals and hence overestimates their densities (*96*). A pressure correction of ~ +1.5 GPa is required to bring the LDA results into agreement with the experimental data. In contrast, the GGA underestimates the density of silicate minerals, and it was suggested that the pressure correction should be at least -2.5 GPa to match the literature data (*100*).

The density of MORB melt with 4.9 wt.% water ranges from 2.902 g/cm^3 at 2.2 GPa to 3.638 g/cm^3 at 13.5 GPa, 1700 K. Compared with dry MORB melt, the density of this hydrous MORB melt is lowered by ~ 0.18 g/cm^3, corresponding to a decrease

of 0.037 g/cm^3 per 1 wt.% H_2O. Recently, Drewitt et al. (*100*) conducted FPMD simulations on MgO-SiO_2-H_2O melts using GGA and found that the incorporation of 1.0 wt.% water can reduce the density of $MgSiO_3$ melt by ~0.043 g/cm^3, which is similar to our results.

The density of MORB melt with 5.3 wt.% CO_2 is lower than that of dry MORB melt but higher than that of MORB melt with 4.9 wt.% H_2O (Table S6). The incorporation of CO_2 into MORB melt also decreases its density, the CO_2 effect on is weaker than the H_2O effect. In comparison, the density of MORB melt only decreases by ~0.015 g/cm^3 per 1 wt.% CO_2. Such a magnitude is similar to the CO_2 effect on the density of pyrolite melt at 3000 K calculated by FPMD simulations using GGA (*101, 102*).

Our simulations together with previous studies on diamond show that diamond is always denser than MORB deeper than the bottom of upper mantle (~12-14 GPa). As the density of silicate melt increases with Fe content but decreases with H_2O and CO_2 contents, the intersection of the density lines of diamond and silicate melt could be changed by 1-2 GPa. This variation caused by the chemical composition does not change the conclusion that diamonds formed in deep-sourced carbon-bearing silicate melts via the redox reaction will descend to the bottom of melt and the residual melt, if it is separated from diamonds, would be enriched in Fe^{3+}.

Supplementary Section 6

The amount of carbon storage

In order to estimate the area of Cenozoic basalt exposed on the land of eastern China, Chen et al. (*51*) utilized a digital-image processing program to extract the distribution information of Cenozoic basalts by pixel from the geological map, and overlaid on the high-precision geomorphologic map. The specific methods are as follows.

The geological and geomorphic map of eastern China attached in GeoMapApp are drawn by Mercator projection. The ratio of basalt eruption area S1 to the Earth surface area S of the region is equal to the ratio of basalt image area P1 in the Mercator projection graph to the image area P of the region, within the latitude of 1 °, between a certain longitude.

$$\frac{S_1}{S} = \frac{P_1}{P}$$

The image area in the Mercator projection graph can be calculated by photoshop software. The Earth surface area S between latitude λ_1 to latitude λ_2 ($\lambda_2 = \lambda_1 + 1$) and longitude ϕ_1 to longitude ϕ_2 ($\phi_2 > \phi_1$) can be obtained by spherical calculation formula:

$$S = 2\pi R^2(\sin\lambda_2 - \sin\lambda_1) \times \frac{(\phi_2 - \phi_1)}{360}$$

Therefore, the basalt eruption area S_1 can be calculated as

$$S_1 = \frac{P_1}{P} 2\pi R^2 (\sin\lambda_2 - \sin\lambda_1) \times \frac{(\phi_2 - \phi_1)}{360}$$

where *R* represents Earth's radius, with an average value of 6371 km. The total area of basalt in a certain area (S_{total}) is the sum of the areas in each latitude.

$$S_{total} = S_1 + S_2 + S_3 + \cdots S_n$$

The results show that the total area of Cenozoic basalts in eastern China is 78525 ± 3141 km^2 (*51*). The carbon stored at the bottom of the BMW, $C_{storage}$, can be calculated according to

$$C_{storage} = S_{total} \times h \times \rho \times C^{4+}$$

where h is thickness of EC basalt, ρ is the density of basalt, and C^{4+} is the amount of carbon required to elevate the average $Fe^{3+}/\sum Fe$ value of MORBs to what is observed in EC basalts via reaction of $4Fe^{2+} + C^{4+} \rightarrow 4Fe^{3+} + C^0$. We assume that the FeO_{total} content of EC basalt is 12 wt%, the density of basalt is 2.9 g/cm^3, and the thickness of EC basalt is ~10 km. To elevate the melt's $Fe^{3+}/\sum Fe$ from a MORB-like value 0.14 (*18*) to 0.35, the average of studied EC basalts (< 50 Ma), the $C_{storage}$ is roughly estimated to be 2400 Gt, which is four times of pre-industrial atmospheric carbon budget (Fig. S11). Note that the measured $Fe^{3+}/\sum Fe$ of EC basalts may represent a minimum value, because $Fe^{3+}/\sum Fe$ of EC basalts may be lowered as they ascended and percolated across the redox melting frontline (~250 km) through the redox melting reaction ($4Fe^{3+} + C^0 \rightarrow 4Fe^{2+} + C^{4+}$).

Supplementary Section 7

The data sources of HIMU lavas (St. Helena and Cook-Austral) used in Fig. 1 in the main text are listed in data file S1.

The arc basalt data used in Fig. 3 in the main text are taken from GEOROC (http://georoc.mpch-mainz.gwdg.de/georoc/Entry.html), with data sources listed in data file S2.

The best estimated 'most parental' $Fe^{3+}/\sum Fe$ values for OIB from each hotspot location used in Figs. 3 and 4 are from Brounce et al. (*19*), with original data from Hartley et al. (*103*), Shorttle et al. (*24*) (Iceland), Helz et al. (*104*), Brounce et al. (*105*), Moussallam et al. (*32*) (Hawaii), Moussallam et al. (*20*) (Erebus), Moussallam et al. (*2*) (Canaries and Cape Verde), Brounce et al. (*19*) and Gaborieau et al. (*106*) (Reunion). Elemental data source of OIB are provided in data file S3. In order to minimize crystal fractionation/accumulation effects, OIB data are filtered by using lavas with MgO between 8% and 16%.

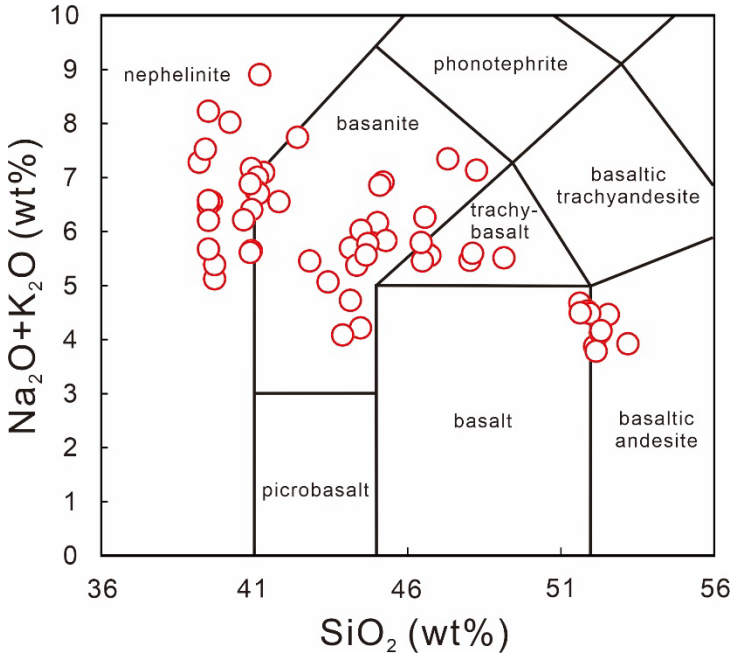

Fig. S1.

Total alkali ($Na_2O + K_2O$) vs SiO_2 diagram for Cenozoic intraplate basalts from eastern China.

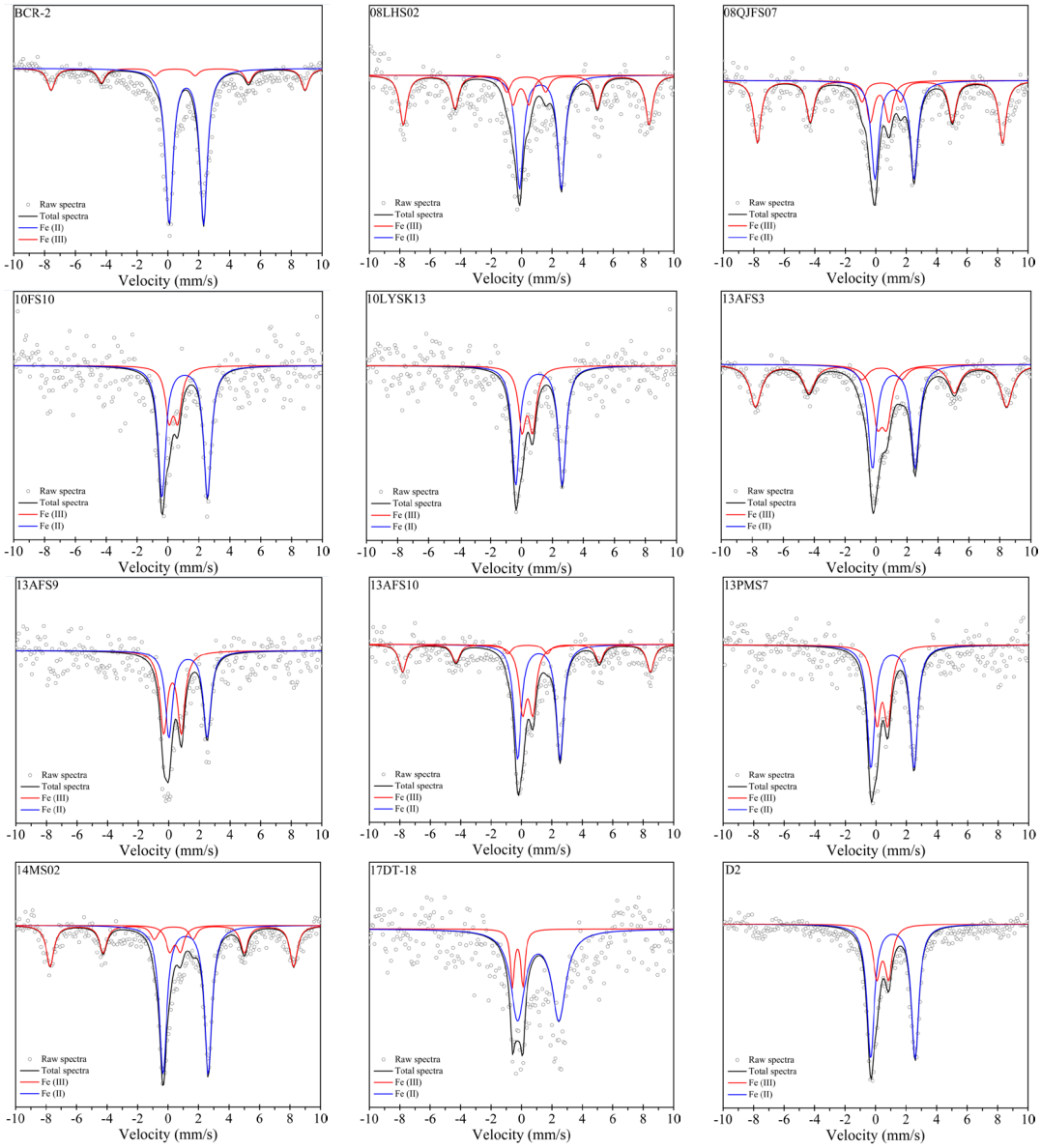

Fig. S2.

Mössbauer spectra measured at 12 K on all analyzed samples.

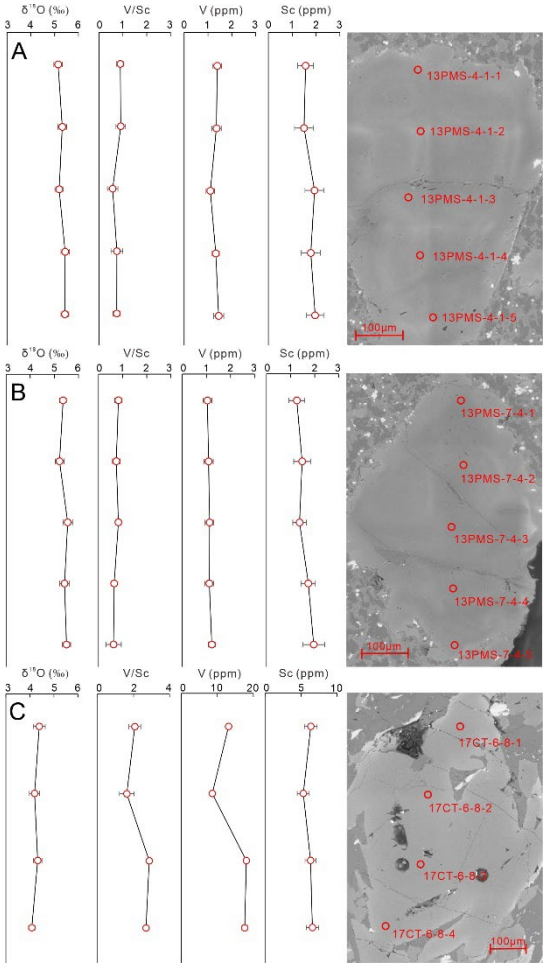

Fig. S3.

$\delta^{18}O$ values, V/Sc ratios, V and Sc content of different positions in olivine phenocrysts for Cenozoic intraplate basalts from eastern China. Data are reported in Table S4.

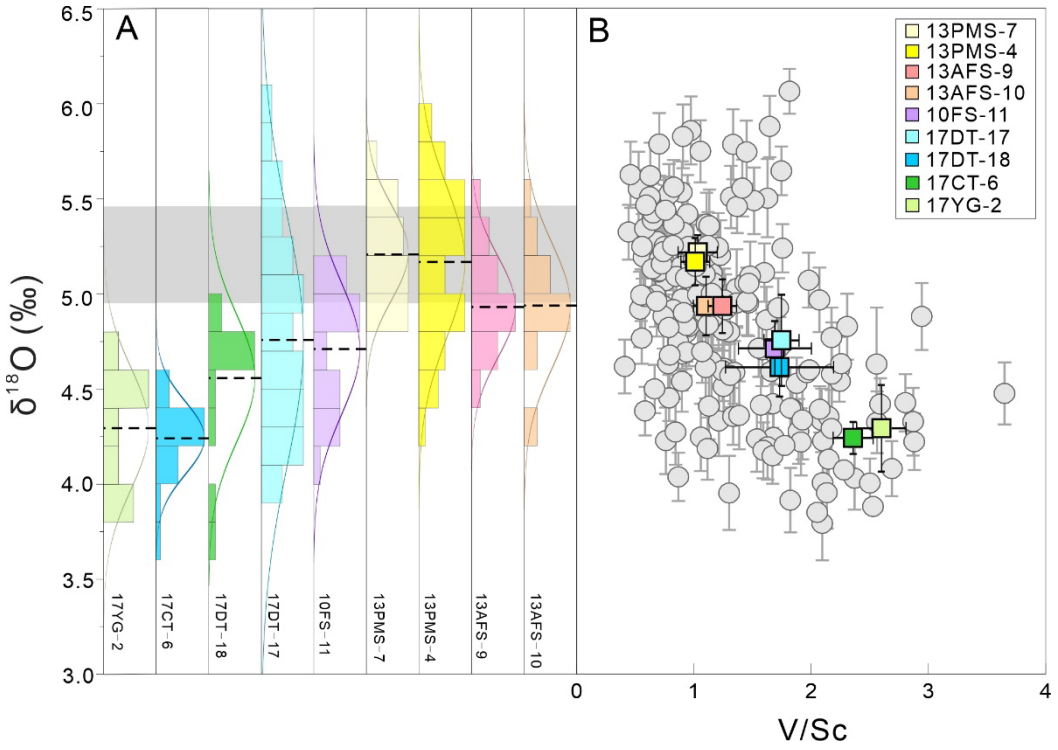

Fig. S4.

All analyzed olivine $\delta^{18}O$ and V/Sc in this study. (**A**) Probability distribution plots of oxygen isotope composition of olivine grains in each individual sample. The black dashed lines represent average $\delta^{18}O$ values for each probability distribution plot. Grey band represents the normal-mantle $\delta^{18}O$ value (5.18 ± 0.28 ‰) (*21*). (**B**) Covariation diagram of $\delta^{18}O$ versus V/Sc in olivine (n=198). Squares represent the average value of different samples. Error bars represent 2 s.e. Data are from Table S4.

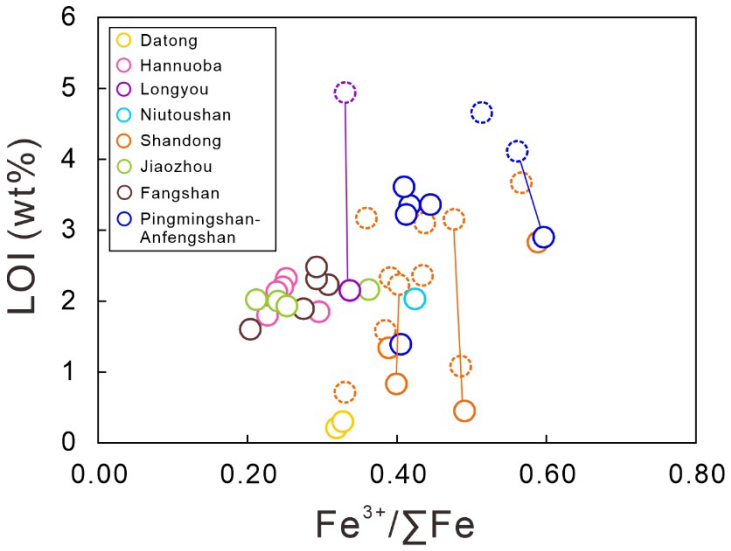

Fig. S5.

Measured $Fe^{3+}/\Sigma Fe$ versus Loss of Ignition (LOI) for Cenozoic intraplate basalts from eastern China in different locations. The iddingsitized samples are shown in dashed outline. Fresh and iddingsitized samples from the same location are connected by lines. Note that the absence of correlation between $Fe^{3+}/\Sigma Fe$ and LOI, and no significant difference between fresh and iddingsitized samples, suggest that surface weathering (*e.g.,* iddingsitization) does not have a large impact on the bulk rock $Fe^{3+}/\Sigma Fe$ values.

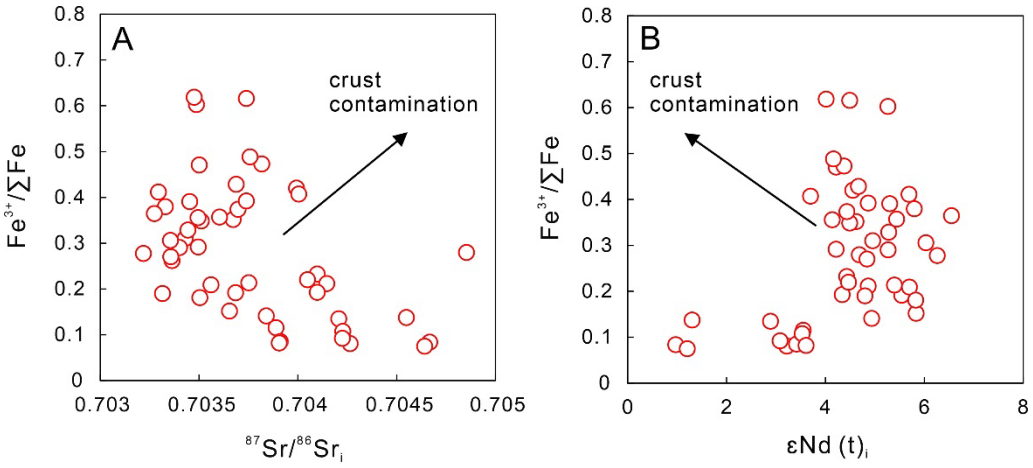

Fig. S6.

Corrected $Fe^{3+}/\Sigma Fe$ values versus $^{87}Sr/^{86}Sr_i$ (A) and $\varepsilon_{Nd}(t)_i$ (B) for Cenozoic intraplate basalts from eastern China (EC). Sr-Nd isotopic compositions were reported in Wang and Liu (*77*) and Li et al. (*16*) and references therein. The relationships preclude crustal contamination or assimilation and fractional crystallization (AFC) processes as the cause of elevated $Fe^{3+}/\Sigma Fe$ for the EC basalts.

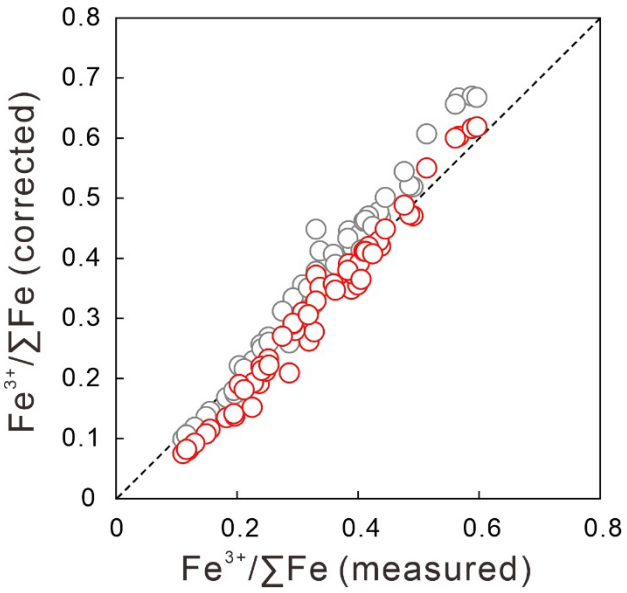

Fig. S7.

Olivine fractional crystallization or accumulation correction of $Fe^{3+}/\Sigma Fe$ for Cenozoic intraplate basalts from eastern China compared with the measured $Fe^{3+}/\Sigma Fe$ value. Data are from Table S1. Samples equilibrium with mantle olivine at Fo_{90} are shown in red circles, and samples equilibrium with mantle olivine at Fo_{85} are shown in grey circles. Correction details are in the Supplementary Section 2.

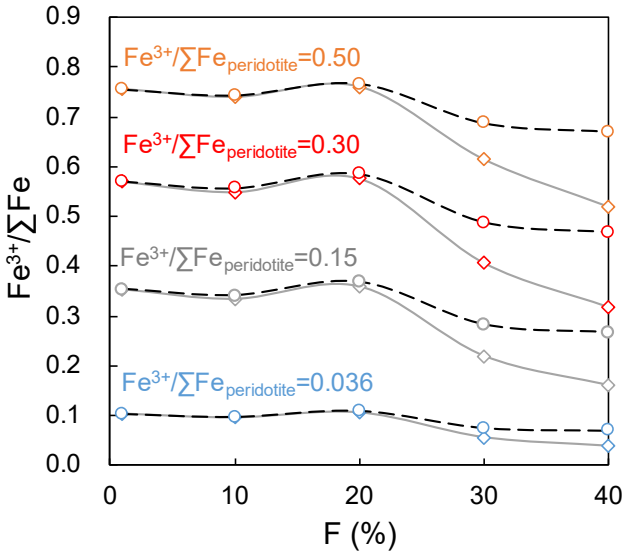

Fig. S8.

The $Fe^{3+}/\Sigma Fe$ of melts generated by batch (black dashed line) and fractional (grey solid line) partial melting of peridotites with different $Fe^{3+}/\Sigma Fe$. The peridotite sources are assumed to have initial $Fe^{3+}/\Sigma Fe$ of 0.036 (normal-mantle value) (*28*), 0.15, 0.30 and 0.50, respectively.

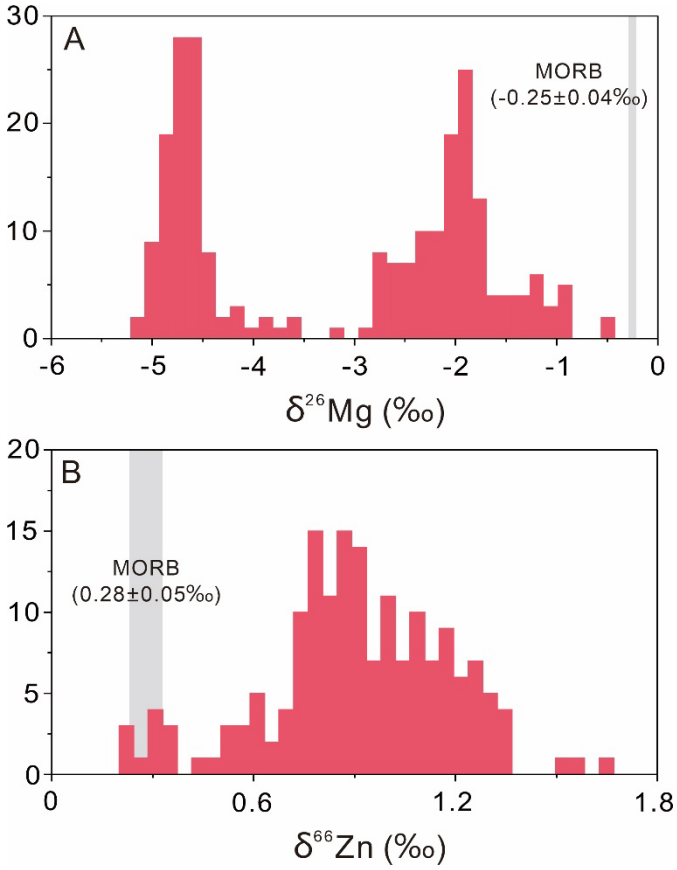

Fig. S9.

Magnesium (A) and Zinc (B) isotopic compositions of sedimentary carbonates compared to those of average MORB. δ^{26}Mg of sedimentary carbonates are compiled from Pokrovsky et al. (*107*), Geske et al. (*108*), Higgins and Schrag (*109-111*), Fantle and Higgins (*112*) and Blättler et al. (*113*). δ^{66}Zn of sedimentary carbonates are compiled from Pichat et al. (*114*), Liu et al. (*115*) and Sweere et al. (*116*). δ^{26}Mg and δ^{66}Zn of MORB shown in grey bar are from Teng et al. (*41*) and Chen et al. (*117*), respectively.

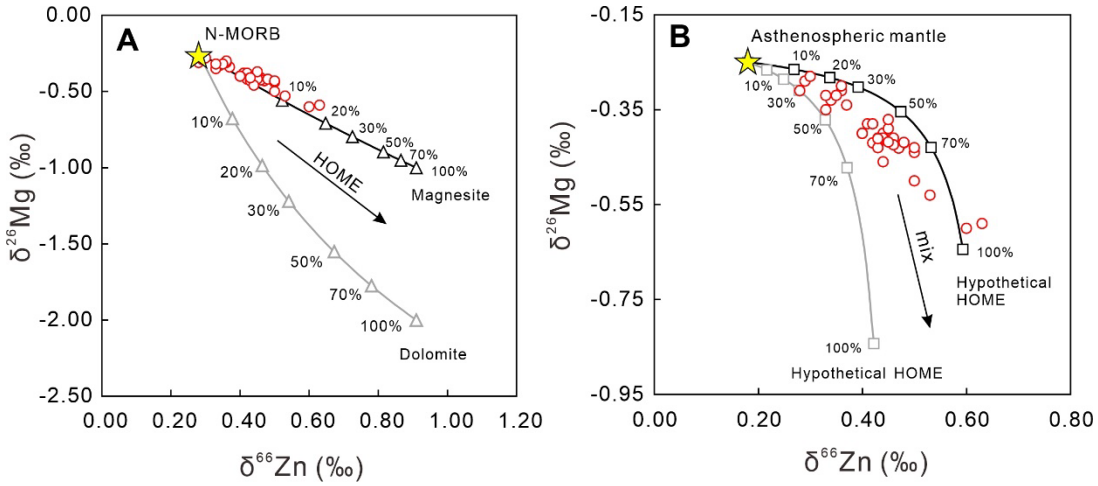

Fig. S10.

Plots of δ^{26}Mg against δ^{66}Zn for the intraplate basalts from eastern China, together with MORB-carbonate mixing (A) and asthenospheric mantle-HOME mixing model (B). Two carbonate species including magnesite (black lines) and dolomite (grey lines) are considered. Hypothetical HOME in (B) is formed by hybridization of 15% carbonate and 85% N-MORB. Modelling parameters are provided in Supplementary Table 7.

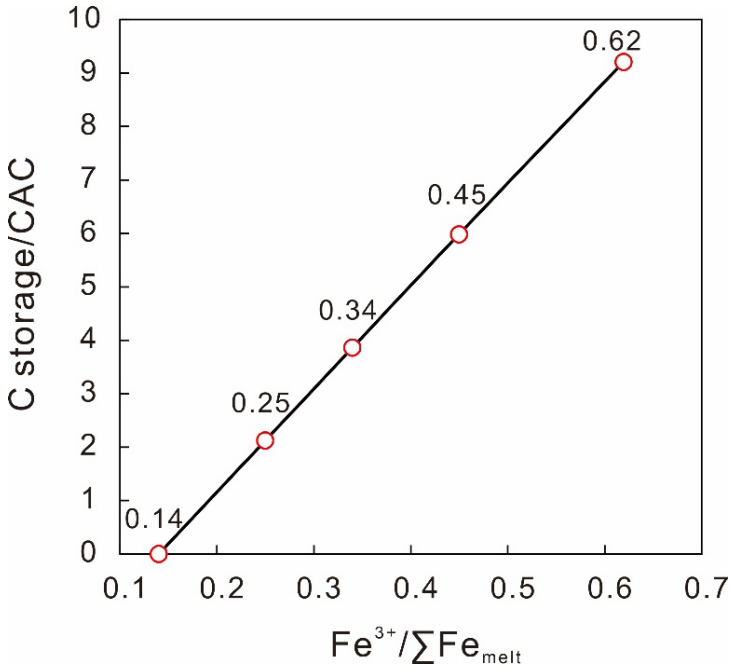

Fig. S11.

The total amount of carbon storage ($C_{storage}$) relative to the current atmospheric carbon (CAC) as a function of assumed average $Fe^{3+}/\Sigma Fe$ in Cenozoic intraplate basalts from eastern China. Computation details are in the Supplementary Section 6.

Legends for Table S1 to S7

Table S1. Wet-chemical Fe^{3+}/Fe_{total} ratios for Cenozoic basalts from eastern China.

Table S2. Wet-chemical determination of FeO content in geological standards.

Table S3. Mössbauer spectroscopic measurements on samples at ~12 K and comparison with wet-chemical measurements.

Table S4. Oxygen isotope and V/Sc ratio of olivine in intraplate basalts from eastern China.

Table S5. The chemical compositions of modeled basaltic melts compared with those of molten basalt investigated by experiments and mid-ocean ridge basalt.

Table S6. The calculated density of three basaltic melts.

Table S7. Parameters used for mixing model.

Legends for data files S1 to S3

Data File S1 Data sources of HIMU lavas.

Data File S2 Data sources of arc basalts compiled from GEOROCK.

Data File S3 Data sources of OIB lavas from each hotspot locations.

REFERENCES AND NOTES

1. D. J. Frost, C. A. McCammon, The redox state of Earth's mantle. *Annu. Rev. Earth Planet. Sci.* **36**, 389–420 (2008).

2. Y. Moussallam, M.-A. Longpré, C. McCammon, A. Gomez-Ulla, E. F. Rose-Koga, B. Scaillet, N. Peters, E. Gennaro, R. Paris, C. Oppenheimer, Mantle plumes are oxidised. *Earth Planet. Sci. Lett.* **527**, 115798 (2019).

3. Y. S. He, X. Meng, S. Ke, H. Wu, C. Zhu, F.-Z. Teng, J. Hoefs, J. Huang, W. Yang, L. Xu, Z. Hou, Z.-Y. Ren, S. Li, A nephelinitic component with unusual δ^{56}Fe in Cenozoic basalts from eastern China and its implications for deep oxygen cycle. *Earth Planet. Sci. Lett.* **512**, 175–183 (2019).

4. R. W. Nicklas, R. K. M. Hahn, L. N. Willhite, M. G. Jackson, V. Zanon, R. Arevalo, J. M. D. Day, Oxidized mantle sources of HIMU- and EM-type Ocean Island Basalts. *Chem. Geol.* **602**, 120901 (2022).

5. S. C. Huang, O. Tschauner, S. Y. Yang, M. Humayun, W. J. Liu, S. N. Gilbert Corder, H. A. Bechtel, J. Tischler, HIMU geochemical signature originating from the transition zone. *Earth Planet. Sci. Lett.* **542**, 116323 (2020).

6. E. S. Kiseeva, D. M. Vasiukov, B. J. Wood, C. McCammon, T. Stachel, M. Bykov, E. Bykova, A. Chumakov, V. Cerantola, J. W. Harris, L. Dubrovinsky, Oxidized iron in garnets from the mantle transition zone. *Nat. Geosci.* **11**, 144–147 (2018).

7. A. Rohrbach, M. W. Schmidt, Redox freezing and melting in the Earth's deep mantle resulting from carbon-iron redox coupling. *Nature* **472**, 209–212 (2011).

8. R. B. Tao, Y. W. Fei, Recycled calcium carbonate is an efficient oxidation agent under deep upper mantle conditions. *Commun. Earth Environ.* **2**, 45 (2021).

9. J. L. Huang, D. P. Zhao, High-resolution mantle tomography of China and surrounding regions. *J. Geophys. Res.* **111**, B09305 (2006).

10. E. Ohtani, D. Zhao, The role of water in the deep upper mantle and transition zone: Dehydration of stagnant slabs and its effects on the big mantle wedge. *Russ. Geol. Geophys.* **50**, 1073–1078 (2009).

11. S. G. Li, Y. Wang, Formation time of the big mantle wedge beneath eastern China and a new lithospheric thinning mechanism of the North China craton-Geodynamic effects of deep recycled carbon. *Sci. China Earth Sci.* **61**, 853–868 (2018).

12. Q. Ma, Y.-G. Xu, Magmatic perspective on subduction of Paleo-Pacific plate and initiation of big mantle wedge in East Asia. *Earth Sci. Rev.* **213**, 103473 (2021).

13. Y. Xu, H. Li, L. Hong, L. Ma, Q. Ma, M. Sun, Generation of Cenozoic intraplate basalts in the big mantle wedge under eastern Asia. *Sci. China Earth Sci.* **61**, 869–886 (2018).

14. R. Xu, Y. Liu, X.-C. Wang, S. F. Foley, Y. Zhang, H. Yuan, Generation of continental intraplate alkali basalts and implications for deep carbon cycle. *Earth Sci. Rev.* **201**, 103073 (2020).

15. G. Zeng, L. H. Chen, X. S. Xu, S. Y. Jiang, A. W. Hofmann, Carbonated mantle sources for Cenozoic intra-plate alkaline basalts in Shandong, North China. *Chem. Geol* **273**, 35–45 (2010).

16. S. G. Li, W. Yang, S. Ke, X. Meng, H. Tian, L. J. Xu, Y. S. He, J. Huang, X. C. Wang, Q. Xia, W. D. Sun, X. Y. Yang, Z. Y. Ren, H. Q. Wei, Y. S. Liu, F. C. Meng, J. Yan, Deep carbon cycles constrained by a large-scale mantle Mg isotope anomaly in eastern China. *Nat. Sci. Rev.* **4**, 111–120 (2017).

17. Y. Liu, S. Gao, P. B. Kelemen, W. Xu, Recycled crust controls contrasting source compositions of Mesozoic and Cenozoic basalts in the North China Craton. *Geochim. Cosmochim. Acta* **72**, 2349–2376 (2008).

18. H. L. Zhang, E. Cottrell, P. A. Solheid, K. A. Kelley, M. M. Hirschmann, Determination of $Fe^{3+}/\Sigma Fe$ of XANES basaltic glass standards by Mössbauer spectroscopy and its application to the oxidation state of iron in MORB. *Chem. Geol.* **479**, 166–175 (2018).

19. M. Brounce, E. Stolper, J. Eiler, The mantle source of basalts from Reunion Island is not more oxidized than the MORB source mantle. *Contrib. Mineral. Petrol.* **177**, 7 (2021).

20. Y. Moussallam, C. Oppenheimer, B. Scaillet, F. Gaillard, P. Kyle, N. Peters, M. Hartley, K. Berlo, A. Donovan, Tracking the changing oxidation state of Erebus magmas, from mantle to surface, driven by magma ascent and degassing. *Earth Planet. Sci. Lett.* **393**, 200–209 (2014).

21. D. Mattey, D. Lowry, C. Macpherson, Oxygen isotope composition of mantle peridotite. *Earth Planet. Sci. Lett.* **128**, 231–241 (1994).

22. C. T. A. Lee, W. P. Leeman, D. Canil, Z. X. A. Li, Similar V/Sc systematics in MORB and arc basalts: Implications for the oxygen fugacities of their mantle source regions. *J. Petrol.* **46**, 2313–2336 (2005).

23. K. A. Kelley, E. Cottrell, The influence of magmatic differentiation on the oxidation state of Fe in a basaltic arc magma. *Earth Planet. Sci. Lett.* **329**, 109–121 (2012).

24. O. Shorttle, Y. Moussallam, M. E. Hartley, J. Maclennan, M. Edmonds, B. J. Murton, Fe-XANES analyses of Reykjanes Ridge basalts: Implications for oceanic crust's role in the solid Earth oxygen cycle. *Earth Planet. Sci. Lett.* **427**, 272–285 (2015).

25. Y. Moussallam, G. Georgeais, E. F. Rose-Koga, K. T. Koga, M. E. Hartley, B. Scaillet, C. Oppenheimer, N. Peters, CO_2-undersaturated melt inclusions from the South West Indian Ridge record surprisingly uniform redox conditions. *Geochem. Geophys. Geosyst.* **24**, e2023GC011235 (2023).

26. G. A. Gaetani, The behavior of $Fe^{3+}/\sum Fe$ during partial melting of spinel lherzolite. *Geochim. Cosmochim. Acta* **185**, 64–77 (2016).

27. E. Cottrell, S. K. Birner, M. Brounce, F. A. Davis, L. E. Waters, K. A. Kelley, “Oxygen fugacity across tectonic settings” in *Magma Redox Geochemistry*, R. Moretti, D. R. Neuville, Eds. (Wiley, 2021), pp. 33–61.

28. D. Canil, H. S. C. O'Neill, D. G. Pearson, R. L. Rudnick, W. F. McDonough, D. A. Carswell, Ferric iron in peridotites and mantle oxidation-states. *Earth Planet. Sci. Lett.* **123**, 205–220 (1994).

29. Y. Moussallam, C. Oppenheimer, A. Aiuppa, G. Giudice, M. Moussallam, P. Kyle, Hydrogen emissions from Erebus volcano, Antarctica. *Bull. Volcanol.* **74**, 2109–2120 (2012).

30. F. Gaillard, B. Scaillet, M. Pichavant, G. Iacono-Marziano, The redox geodynamics linking basalts and their mantle sources through space and time. *Chem. Geol.* **418**, 217–233 (2015).

31. R. Moretti, D. R. Neuville, Eds. *Magma Redox Geochemistry* (American Geophysical Union, Wiley, 2021).

32. Y. Moussallam, M. Edmonds, B. Scaillet, N. Peters, E. Gennaro, I. Sides, C. Oppenheimer, The impact of degassing on the oxidation state of basaltic magmas: A case study of Kīlauea volcano. *Earth Planet. Sci. Lett.* **450**, 317–325 (2016).

33. S. Ding, T. Plank, P. J. Wallace, D. J. Rasmussen, Sulfur_X: A model of sulfur degassing during magma ascent. *Geochem. Geophys. Geosyst.* **24**, e2022GC010552 (2023).

34. D. Canil, Vanadium partitioning and the oxidation state of Archaean komatiite magmas. *Nature* **389**, 842–845 (1997).

35. S. F. Foley, D. Prelevic, T. Rehfeldt, D. E. Jacob, Minor and trace elements in olivines as probes into early igneous and mantle melting processes. *Earth Planet. Sci. Lett.* **363**, 181–191 (2013).

36. K. A. Kelley, E. Cottrell, Water and the oxidation state of subduction zone magmas. *Science* **325**, 605–607 (2009).

37. T. Kogiso, Y. Tatsumi, S. Nakano, Trace element transport during dehydration processes in the subducted oceanic crust: 1. Experiments and implications for the origin of ocean island basalts. *Earth Planet. Sci. Lett.* **148**, 193–205 (1997).

38. M. J. Walter, G. P. Bulanova, L. S. Armstrong, S. Keshav, J. D. Blundy, G. Gudfinnsson, O. T. Lord, A. R. Lennie, S. M. Clark, C. B. Smith, L. Gobbo, Primary carbonatite melt from deeply subducted oceanic crust. *Nature* **454**, 622–625 (2008).

39. S. A. Liu, Z. Z. Wang, S. G. Li, J. Huang, W. Yang, Zinc isotope evidence for a large-scale carbonated mantle beneath eastern China. *Earth Planet. Sci. Lett.* **444**, 169–178 (2016).

40. F. Moynier, D. Vance, T. Fujii, P. Savage, The isotope geochemistry of zinc and copper. *Rev. Miner. Geochem.* **82**, 543–600 (2017).

41. F. Teng, Z., Magnesium isotope geochemistry. *Rev. Mineral. Geochem.* **82**, 219–287 (2017).

42. A. R. Thomson, M. J. Walter, S. C. Kohn, R. A. Brooker, Slab melting as a barrier to deep carbon subduction. *Nature* **529**, 76–79 (2016).

43. M. A. Kendrick, J. X. Zhao, Y. X. Feng, Early accretion and prolonged carbonation of the Pacific Ocean's oldest crust. *Geology* **50**, 1270–1275 (2022).

44. J. C. Alt, D. A. H. Teagle, Hydrothermal alteration of upper oceanic crust formed at a fast-spreading ridge: Mineral, chemical, and isotopic evidence from ODP Site 801. *Chem. Geol.* **201**, 191–211 (2003).

45. Y. Weiss, C. Class, S. L. Goldstein, T. Hanyu, Key new pieces of the HIMU puzzle from olivines and diamond inclusions. *Nature* **537**, 666–670 (2016).

46. J. Y. Xu, A. Giuliani, Q. L. Li, K. Lu, J. C. Melgarejo, W. L. Griffin, Light oxygen isotopes in mantle-derived magmas reflect assimilation of sub-continental lithospheric mantle material. *Nat. Commun.* **12**, 6295 (2021).

47. X. C. Wang, S. A. Wilde, Q. L. Li, Y. N. Yang, Continental flood basalts derived from the hydrous mantle transition zone. *Nat. Commun.* **6**, 7700 (2015).

48. A. Rohrbach, C. Ballhaus, U. Golla-Schindler, P. Ulmer, V. S. Kamenetsky, D. V. Kuzmin, Metal saturation in the upper mantle. *Nature* **449**, 456–458 (2007).

49. S. E. Mazza, E. Gazel, M. Bizimis, R. Moucha, P. Beguelin, E. A. Johnson, R. J. McAleer, A. V. Sobolev, Sampling the volatile-rich transition zone beneath Bermuda. *Nature* **569**, 398–403 (2019).

50. P. R. Castillo, The recycling of marine carbonates and sources of HIMU and FOZO ocean island basalts. *Lithos* **216-217**, 254–263 (2015).

51. X. Y. Chen, L. H. Chen, Y. Chen, G. Zeng, J. Q. Liu, Distribution summary of Cenozoic basalts in Central and Eastern China. *Geol. J. China Univ.* **20**, 507–519 (2014).

52. V. Stagno, D. O. Ojwang, C. A. McCammon, D. J. Frost, The oxidation state of the mantle and the extraction of carbon from Earth's interior. *Nature* **493**, 84–88 (2013).

53. S. F. Foley, “Redox melting in the mantle” in *Magma Redox Geochemistry*, R. Moretti, D. R. Neuville, Eds. (Wiley, 2021), pp. 93–113.

54. Y. Fukao, M. Obayashi, Subducted slabs stagnant above, penetrating through, and trapped below the 660 km discontinuity. *J. Geophys. Res. Solid Earth* **118**, 5920–5938 (2013).

55. M. Yin, J. X. Li, Eds. *Analysis of Rock and Minerals* (Geological Publishing House, 2011), vol. **2**, pp. 1–862.

56. P. A. Sossi, J. D. Foden, G. P. Halverson, Redox-controlled iron isotope fractionation during magmatic differentiation: An example from the Red Hill intrusion, S. Tasmania. *Contrib. Mineral. Petrol.* **164**, 757–772 (2012).

57. A. Kumar, M. R. Singh, P. R. Sarma, K. C. Tripathi, Optimised thickness of diffusive Mossbauer absorbers. *J. Phys. D Appl. Phys.* **22**, 465–466 (1989).

58. A. Thompson, D. G. Rancourt, O. A. Chadwick, J. Chorover, Iron solid-phase differentiation along a redox gradient in basaltic soils. *Geochim. Cosmochim. Acta* **75**, 119–133 (2011).

59. T. Mansfeldt, S. Schuth, W. Hausler, F. E. Wagner, S. Kaufhold, M. Overesch, Iron oxide mineralogy and stable iron isotope composition in a Gleysol with petrogleyic properties. *J. Soil Sedim.* **12**, 97–114 (2012).

60. J. M. Eiler, C. Graham, J. W. Valley, SIMS analysis of oxygen isotopes: Matrix effects in complex minerals and glasses. *Chem. Geol.* **138**, 221–244 (1997).

61. F. Guo, J. T. Guo, C. Y. Wang, W. M. Fan, C. W. Li, L. Zhao, H. X. Li, J. Y. Li, Formation of mafic magmas through lower crustal AFC processes - An example from the Jinan gabbroic intrusion in the North China Block. *Lithos* **179**, 157–174 (2013).

62. J. Eiler, E. M. Stolper, M. C. McCanta, Intra- and intercrystalline oxygen isotope variations in minerals from basalts and peridotites. *J. Petrol.* **52**, 1393–1413 (2011).

63. 63. N . T. Kita, T. Ushikubo, B. Fu, M. J. Spicuzza, J. W. Valley, Analytical developments on oxygen three isotope analyses using a new generation ion microprobe IMS-1280, in *38th Lunar and Planetary science Conference*, Abstract 1981 (2007).

64. I. Bindeman, A. Gurenko, O. Sigmarsson, M. Chaussidon, Oxygen isotope heterogeneity and disequilibria of olivine crystals in large volume Holocene basalts from Iceland: Evidence for magmatic digestion and erosion of Pleistocene hyaloclastites. *Geochim. Cosmochim. Acta* **72**, 4397–4420 (2008).

65. A. A. Gurenko, I. N. Bindeman, M. Chaussidon, Oxygen isotope heterogeneity of the mantle beneath the Canary Islands: Insights from olivine phenocrysts. *Contrib. to Mineral. Petrol.* **162**, 349–363 (2011).

66. S. T. Wu, G. Wörner, K. P. Jochum, B. Stoll, K. Simon, A. Kronz, The preparation and preliminary characterisation of three synthetic andesite reference glass materials (ARM-1, ARM-2, ARM-3) for in situ microanalysis. *Geostand. Geoanal. Res.* **43**, 567–584 (2019).

67. V. G. Batanova, J. M. Thompson, L. V. Danyushevsky, M. V. Portnyagin, D. Garbe-Schonberg, E. Hauri, J. I. Kimura, Q. Chang, R. Senda, K. Goemann, C. Chauvel, S. Campillo, D. A. Ionov, A. V. Sobolev, New olivine reference material for in situ microanalysis. *Geostand. Geoanal. Res.* **43**, 453–473 (2019).

68. S. T. Wu, Y. D. Wu, Y. H. Yang, H. Wang, C. Huang, L. W. Xie, J. H. Yang, Simultaneous quantification of forsterite content and minor-trace elements in olivine by LA-ICP-MS and geological applications in Emeishan large igneous province. *Minerals-Basel* **10**, 634 (2020).

69. W. F. McDonough, S. S. Sun, The composition of the Earth. *Chem. Geol.* **120**, 223–253 (1995).

70. R. L. Rudnick, S. Gao, “Composition of the continental crust” in *Treatise on Geochemistry*, H. D. Holland, K. K. Turekian, Eds. (Pergamon, 2003), vol. **3**, pp. 1–64.

71. Y. Weiss, W. L. Griffin, D. R. Bell, O. Navon, High-Mg carbonatitic melts in diamonds, kimberlites and the sub-continental lithosphere. *Earth Planet. Sci. Lett.* **309**, 337–347 (2011).

72. K. Hoernle, G. Tilton, M. J. Le Bas, S. Duggen, D. Garbe-Schönberg, Geochemistry of oceanic carbonatites compared with continental carbonatites: Mantle recycling of oceanic crustal carbonate. *Contrib. Mineral. Petrol.* **142**, 520–542 (2002).

73. J. W. Valley, M. J. Spicuzza, T. Ushikubo, Correlated $\delta^{18}O$ and [Ti] in lunar zircons: A terrestrial perspective for magma temperatures and water content on the Moon. *Contrib. Miner. Petrol.* **167**, 956 (2014).

74. A. Fitzpayne, A. Giuliani, J. Hergt, D. Phillips, P. Janney, New geochemical constraints on the origins of MARID and PIC rocks: Implications for mantle metasomatism and mantle-derived potassic magmatism. *Lithos* **318-319**, 478–493 (2018).

75. M. Massuyeau, X. Ritter, C. Sanchez-Valle, A density model for high-pressure carbonate-rich melts applied to carbonatitic magmatism in the upper mantle. *Chem. Geol.* **622**, 121275 (2022).

76. R. Dasgupta, Ingassing, storage, and outgassing of terrestrial carbon through geologic time. *Rev. Miner. Geochem.* **75**, 183–229 (2013).

77. Z. Z. Wang, S. A. Liu, Evolution of intraplate alkaline to tholeiitic basalts via interaction between carbonated melt and lithospheric mantle. *J. Petrol.* **62**, 1–25 (2021).

78. S. P. Qian, Z. Y. Ren, L. Zhang, L. B. Hong, J. Q. Liu, Chemical and Pb isotope composition of olivine-hosted melt inclusions from the Hannuoba basalts, North China Craton: Implications for petrogenesis and mantle source. *Chem. Geol.* **401**, 111–125 (2015).

79. G. Zeng, L. H. Chen, A. W. Hofmann, X. J. Wang, J. Q. Liu, X. Yu, L. W. Xie, Nephelinites in eastern China originating from the mantle transition zone. *Chem. Geol.* **576**, 120276 (2021).

80. J. Huang, S.-G. Li, Y. Xiao, S. Ke, W.-Y. Li, Y. Tian, Origin of low $\delta^{26}Mg$ Cenozoic basalts from South China Block and their geodynamic implications. *Geochim. Cosmochim. Acta* **164**, 298–317 (2015).

81. F. C. Meng, T. F. Li, H. M. Xue, F. L. Liu, Z. Q. Xu, Two serials of basic magmas from different mantle sources of Late Cretaceous in east Shandong province, China: A comparative study on basalts from Zhucheng and Jiaozhou. *Acta Petrol. Sin.* **22**, 1644–1656 (2006).

82. J. Yang, "Petrological and geochemical studies of the cenozoic basalts and hosted peridotite xenoliths in Zhejiang and Fujian provinces," thesis, China University of Geosciences (Beijing) (2015).

83. C. Q. Sun, J. Q. Liu, B. Xu, H. T. You, First radiocarbon dating of a Holocene eruption of the Datong volcanic field, eastern China. *J. Volcanol. Geotherm. Res.* **384**, 275–279 (2019).

84. H. Zhao, Z. Liu, C. M. Wang, S. H. Li, Luminescence dating of volcanic eruptions in Datong, northern China. *Quat. Geochronol.* **30**, 357–362 (2015).

85. D. Luo, L. H. Chen, G. Zeng, Genesis of intra-continental strongly alkaline volcanic rocks: A case study of Dashan nephelinites in Wudi, Shandong Province, North China. *Acta Petrol. Sin.* **25**, 311–319 (2009).

86. S. Z. Sheng, S. J. Wang, X. M. Yang, L. H. Chen, G. Zeng, Y. Xiao, J. Shen, X. H. Dong, Y. W. Lv, Sulfide dissolution on the nickel isotopic composition of basaltic rocks. *J. Geophys. Res. Solid Earth* **127**, e2022JB024555 (2022).

87. Z. Z. Wang, S. A. Liu, L. H. Chen, S. G. Li, G. Zeng, Compositional transition in natural alkaline lavas through silica-undersaturated melt–lithosphere interaction. *Geology* **46**, 771–774 (2018).

88. E. Cottrell, K. A. Kelley, The oxidation state of Fe in MORB glasses and the oxygen fugacity of the upper mantle. *Earth Planet. Sci. Lett.* **305**, 270–282 (2011).

89. P. A. Sossi, O. Nebel, J. Foden, Iron isotope systematics in planetary reservoirs. *Earth Planet. Sci. Lett.* **452**, 295–308 (2016).

90. P. L. Roeder, R. F. Emslie, Olivine-liquid equilibrium *Mineral. Petrol.* **29**, 275–289 (1970).

91. A. D. T. Goode, Oxidation of natural olivines. *Nature* **248**, 500–501 (1974).

92. M. J. Walter, Melting of garnet peridotite and the origin of komatiite and depleted lithosphere. *J. Petrol.* **39**, 29–60 (1998).

93. J. Wang, F. Huang, X. Xiong, E. Takahashi, "*Partition Coefficients of Fe^{3+} and Fe^{2+} between Mantle Minerals and Melts: Implications for Redox Variations during Mantle Melting*" (AGU Fall Meeting 2021, New Orleans, LA, 2021).

94. R. Dasgupta, M. M. Hirschmann, The deep carbon cycle and melting in Earth's interior. *Earth Planet. Sci. Lett.* **298**, 1–13 (2010).

95. B. B. Karki, First-principles computation of mantle materials in crystalline and amorphous phases. *Phys. Earth Planet.* **240**, 43–69 (2015).

96. R. Wentzcovitch, Y. G. Yu, Z. Wu, Thermodynamic properties and phase relations in mantle minerals investigated by first principles Quasiharmonic theory. *Rev. Mineral. Geochem.* **71**, 59–98 (2010).

97. W. Wang, Y. Xu, D. Sun, S. Ni, R. Wentzcovitch, Z. Wu, Velocity and density characteristics of subducted oceanic crust and the origin of lower-mantle heterogeneities. *Nat. Commun.* **11**, 64 (2020).

98. R. Caracas, K. Hirose, R. Nomura, M. D. Ballmer, Melt–crystal density crossover in a deep magma ocean. *Earth Planet. Sci. Lett.* **516**, 202–211 (2019).

99. C. B. Agee, Crystal-liquid density inversions in terrestrial and lunar magmas. *Phys. Earth Planet. In.* **107**, 63–74 (1998).

100. J. W. E. Drewitt, M. J. Walter, J. P. Brodholt, J. M. R. Muir, O. T. Lord, Hydrous silicate melts and the deep mantle H_2O cycle. *Earth Planet. Sci. Lett.* **581**, 117408 (2022).

101. N. V. Solomatova, R. Caracas, Buoyancy and structure of volatile-rich silicate melts. *J. Geophys. Res. Solid Earth* **126**, e2020JB021045 (2021).

102. N. V. Solomatova, R. Caracas, C. E. Manning, Carbon sequestration during core formation implied by complex carbon polymerization. *Nat. Commun.* **10**, 789 (2019).

103. M. E. Hartley, O. Shorttle, J. Maclennan, Y. Moussallam, M. Edmonds, Olivine-hosted melt inclusions as an archive of redox heterogeneity in magmatic systems. *Earth Planet. Sci. Lett.* **479**, 192–205 (2017).

104. R. L. Helz, E. Cottrell, M. Brounce, K. A. Kelley, Olivine-melt relationships and syneruptive redox variations in the 1959 eruption of Kīlauea Volcano as revealed by XANES. *J. Volcanol. Geotherm. Res.* **333**, 1–14 (2017).

105. M. Brounce, E. Stolper, J. Eiler, Redox variations in Mauna Kea lavas, the oxygen fugacity of the Hawaiian plume, and the role of volcanic gases in Earth's oxygenation. *Proc. Natl. Acad. Sci. U.S.A.* **114**, 8997–9002 (2017).

106. M. Gaborieau, M. Laubier, N. Bolfan-Casanova, C. A. McCammon, D. Vantelon, A. I. Chumakov, F. Schiavi, D. R. Neuville, S. Venugopal, Determination of $Fe^{3+}/\Sigma Fe$ of olivine-hosted melt inclusions using Mössbauer and XANES spectroscopy. *Chem. Geol.* **547**, 119646 (2020).

107. B. G. Pokrovsky, V. Mavromatis, O. S. Pokrovsky, Co-variation of Mg and C isotopes in late Precambrian carbonates of the Siberian Platform: A new tool for tracing the change in weathering regime? *Chem. Geol.* **290**, 67–74 (2011).

108. A. Geske, J. Zorlu, D. K. Richter, D. Buhl, A. Niedermayr, A. Immenhauser, Impact of diagenesis and low grade metamorphosis on isotope ($\delta^{26}Mg$, $\delta^{13}C$, $\delta^{18}O$ and $^{87}Sr/^{86}Sr$) and elemental (Ca, Mg, Mn, Fe and Sr) signatures of Triassic sabkha dolomites. *Chem. Geol.* **332-333**, 45–64 (2012).

109. J. A. Higgins, D. P. Schrag, Constraining magnesium cycling in marine sediments using magnesium isotopes. *Geochim. Cosmochim. Acta* **74**, 5039–5053 (2010).

110. J. A. Higgins, D. P. Schrag, The Mg isotopic composition of Cenozoic seawater- evidence for a link between Mg-clays, seawater Mg/Ca, and climate. *Earth Planet. Sci. Lett.* **416**, 73–81 (2015).

111. J. A. Higgins, D. P. Schrag, Records of Neogene seawater chemistry and diagenesis in deep-sea carbonate sediments and pore fluids. *Earth Planet. Sci. Lett.* **357**, 386–396 (2012).

112. M. S. Fantle, J. Higgins, The effects of diagenesis and dolomitization on Ca and Mg isotopes in marine platform carbonates: Implications for the geochemical cycles of Ca and Mg. *Geochim. Cosmochim. Acta* **142**, 458–481 (2014).

113. C. L. Blattler, N. R. Miller, J. A. Higgins, Mg and Ca isotope signatures of authigenic dolomite in siliceous deep-sea sediments. *Earth Planet. Sci. Lett.* **419**, 32–42 (2015).

114. S. Pichat, C. Douchet, F. Albarède, Zinc isotope variations in deep-sea carbonates from the eastern equatorial Pacific over the last 175 ka. *Earth Planet. Sci. Lett.* **210**, 167–178 (2003).

115. S. A. Liu, H. C. Wu, S. Z. Shen, G. Q. Jiang, S. H. Zhang, Y. W. Lv, H. Zhang, S. G. Li, Zinc isotope evidence for intensive magmatism immediately before the end-Permian mass extinction. *Geology* **45**, 343–346 (2017).

116. T. C. Sweere, A. J. Dickson, H. C. Jenkyns, D. Porcelli, M. Elrick, S. H. J. M. van den Boorn, G. M. Henderson, Isotopic evidence for changes in the zinc cycle during Oceanic Anoxic Event 2 (Late Cretaceous). *Geology* **46**, 463–466 (2018).

117. H. Chen, P. S. Savage, F.-Z. Teng, R. T. Helz, F. Moynier, Zinc isotope fractionation during magmatic differentiation and the isotopic composition of the bulk Earth. *Earth Planet. Sci. Lett.* **369-370**, 34–42 (2013).